

The Internal Nebular Attenuation Curve of Three-Dimensional Turbulent HII regions

Yifei Jin^{1*}, Yong Shi¹, Ralph Sutherland², Ziyu Huang³, and Chuanfei Dong^{3,4}

¹ Westlake University, 600 Dунyу Road, Xihu District, Hangzhou, Zhejiang 310030 PR China

² Mount Stromlo Observatory, Australian National University, Weston Creek, Canberra, ACT 2611 Australia

³ Department of Astronomy, Boston University, Boston, MA 02215 USA

⁴ School of Natural Sciences, Institute for Advanced Study, Princeton, NJ 08540, USA

Received September 30, 20XX

ABSTRACT

The internal dust attenuation of the HII region reduces the observed emission-line fluxes. Turbulent density fields within each HII region change the degree of the line-of-sight obscuration of the emission-line fluxes. In this paper, we implement the dust Monte-Carlo radiative transfer in the latest M3D code, creating the emission-line maps attenuated by the internal turbulent dust obscuration with the varying Mach numbers. The internal density and temperature fluctuations of HII regions make the radiative transfer of hydrogen lines neither Case A nor Case B conditions, resulting in the global $H\alpha$ to $H\beta$ ratio of approximately 3.02-3.03, differing from the widely-used value of 2.86. This deviation from Case B is because the temperature of these HII regions is cooler than 10,000 K. We further derive the internal nebular attenuation curve from the attenuated Hydrogen lines, finding that the clumpy structures within HII regions do not change the slope of the internal attenuation curve. This is because the heavy dust obscuration of dense clumps is canceled out by the high in-situ production of emission-line intensities.

Key words. Galaxies – Interstellar medium – Interstellar dust extinction – High-redshift galaxies

1. Introduction

Ionized nebulae (HII regions) surrounding young, hot, massive stars are the prominent sites producing the galactic emission-lines. Analyzing the HII region emission-line properties decodes fundamental properties of the interstellar medium and is a key part of understanding the physical parameters of galaxy formation and evolution scenarios. These properties include the gas-phase metallicity (Sanders et al. 2021), the interstellar medium (ISM) pressure/density (Kaasinen et al. 2017) and the spectrum of the ionization field (Veilleux & Osterbrock 1987). The correction for the loss of fluxes caused by the internal dust obscuration is critical to these inferences because the nebular regions are preferentially located in dusty star-forming clouds.

An attenuation curve is adopted to parameterize the wavelength-dependent effect of dust obscuration, in which its shape encodes the complexity of dust properties and the spatially-geometrical relation between the stars and their surrounding dust/gas absorbers (Seon & Draine 2016; Reddy et al. 2020). The nonuniform distribution of dust around stars varies the column density and the covering fraction of the dust obscuration to the stellar continuum and the nebular emission (Caplan & Deharveng 1986).

In an individual nebula, the total nebular spectrum could be dominated by less dust affected, bright [OIII] $\lambda\lambda$ 4959,5007 and $H\beta$ -emitting regions that fill most of the nebular volume, like what is observed in LMC-N59 (Pellegrini et al. 2012). In some cases, the nebular spectrum could be dominated by the reddened line species residing at the edge of nebula, like [SII] $\lambda\lambda$ 6717,31 and [OI] λ 6300. One case is the nebula M16 (Hester et al. 1996),

which may be closely associated with the surfaces of dusty dense clumps (Mellema et al. 2006). In some extreme cases, like DEM 301 (Oey & Kennicutt 1997), the nebular attenuation is absent in the regions where the lines-of-sight allow ionizing photons to escape from the nebula without significant absorption (Pellegrini et al. 2012). In the other extreme case, like ultracompact HII regions (Wood & Churchwell 1989), the nebular emission-lines are heavily embedded in compact dusty clumps where the ionization front is completely neutral (Petrosian et al. 1972). Therefore, the spectrum of a clumpy HII region is the aggregate of many lines of sight through varying attenuation. The integrated light at different wavelengths may be biased to the brighter regions at different optical depths. This is an essential difference between the attenuation of the clumpy and uniform ISM.

The influence of the turbulence in HII regions on the nebular attenuation curve may be at least twofold. On one hand, the dust attenuation depth in the patchy ISM varies in different directions. The dust obscuration is heavier in the directions of the larger column densities, usually with denser clumps along the line of the sight (Zamora-Avilés et al. 2019). On the other hand, the density fluctuation of the ionized gas changes the intrinsic emission-line fluxes by deviating the temperature and ionization structures from the uniform density models within the HII regions. This nonuniform ionization structure is a seldom-considered factor which cannot be reproduced in a symmetric homogeneous model (Jin et al. 2022b). Substructure is ubiquitous in HII regions as they evolve in their turbulent ambient ISM, so inhomogeneity is inevitable (Elmegreen & Scalo 2004).

Observations and simulations have revealed that the importance of the turbulent motion in star-forming galaxies is increasing along the redshift (Wisnioski et al. 2015; Pillepich et al.

* Corresponding author: yfjsci@gmail.com

2019). Especially at high-redshift $z > 2$, the high incidents of galaxy mergers further perturb the turbulence in the ISM (Sparre et al. 2022). The unprecedented Infrared (IR) spectroscopic capability of JWST pushes the frontier of the rest-frame emission-line studies to the very early Universe around $z \sim 12$, opening a new window to understand the interplay between the ISM turbulence and the emission-line behaviors as well as the dust attenuation (Shapley et al. 2025; Reddy et al. 2025).

To begin to test this qualitative description, in this paper, we create a series of turbulent HII regions with varying Mach numbers, and investigate the impact of the turbulent density fluctuation of the ionized gas on the measurement of the nebular attenuation curve. We describe turbulent HII region models in Section 2 and their dust-attenuated hydrogenic-line maps in Section 4. The deduced nebular attenuation curve is reported in Section 5. The conclusion is summarized in Section 7. The purpose of this paper is to demonstrate the impact of the non-uniform turbulent density field on the internal attenuation curve of HII regions.

2. Model

We create a series of HII regions with the turbulent density fields of varying Mach numbers through the following steps. We first run hydrodynamic simulations to create the turbulent boxes with varying Mach numbers. We then illuminate the turbulent boxes using the Monte-Carlo radiative transfer photoionization code to create cubes of nebular emission-lines. The emission-lines are reddened by the dust attenuation that is proportional to the intrinsic density fluctuations of the turbulent box along the line of sight.

2.1. Turbulent Interstellar Medium

We use the ATHENA++ code (Stone et al. 2020) to create the turbulent boxes, which provide the density fields for post-processing. The density fields are characterized by the Mach number and the lowest wavenumber of the turbulent box k_{min} , respectively. The Mach number controls the dispersion of the probability distribution function (PDF) of the gaseous density (Molina et al. 2012). The k parameter defines the maximal periods of the density oscillation along each side of the turbulent boxes, which constrains the largest scale of the turbulent filament in the simulation. The physical domain size is $L = 64$ pc and the simulations are performed on a uniform grid with a resolution of $N^3 = 125 \times 125 \times 125$ cells. The turbulence boxes with different Mach numbers are the selected snapshots from simulations with identical driving, $\dot{E}/\bar{\rho}L^2c_s^3 = 10$, where $\bar{\rho}$ is the average density, L is the size of the domain and c_s is the sound speed. We create the turbulent boxes of the Mach numbers $\mathcal{M} = 0.997, 2.484, 4.739, \text{ and } 8.791$ with the lowest wavenumbers $k_{min} = 4$, and $\mathcal{M} = 0.997, 2.472, 4.856, \text{ and } 8.817$ with the lowest wavenumbers $k_{min} = 9$. The chaos of the gas increases as the time evolving and the energy cascades to the small scale and dissipates at the small eddies. The clumpy and filamentary structures appear during the nonlinear interaction of gas flow. The mean density of the turbulent medium is 10 cm^{-3} .

2.2. Photoionization Models

The M3D code¹ (the updated version of M³, see Jin et al. 2022a) is a self-consistent three-dimensional Monte-Carlo radiative transfer (MCRT) photoionization code designed to create HII re-

gions with arbitrary geometries. It is the descendant of the MAPPINGS project, which was initialized by Dopita (1976) and evolved through the continuous development of Binette et al. (1985); Sutherland & Dopita (1993) and Groves et al. (2004). The M3D code inherits the framework of MAPPINGS V, the most up-to-date version of MAPPINGS code that was restructured by Sutherland et al. (2018), which includes the updated microphysics of the ISM, the efficient strategies of the cooling and heating calculations, and the CHIANTI V.8 atomic data (Del Zanna et al. 2015).

In the latest version of M3D, we consider the absorption and scattering by gas and dust by comparing the total random optical depth, τ_p , with the analytical optical depth, τ_l , over each displacement of l ,

$$\tau_l = (\kappa_{abs}^{gas} + \kappa_{abs}^{dust} + \kappa_{scat}^{dust}) \cdot \rho \cdot l, \quad (1)$$

where κ_{abs}^{gas} , κ_{abs}^{dust} and κ_{scat}^{dust} are the coefficients of gas and dust absorption and dust scattering, and ρ is the gas density. Once the total analytical optical depth is larger than the random optical depth, the photon is then determined to be either scattered or absorbed according to the probability of each event.

$$P_{scat}^{dust} = \frac{\kappa_{scat}^{dust}}{\kappa_{tot}} \quad (2)$$

$$P_{abs}^{gas} = \frac{\kappa_{abs}^{gas}}{\kappa_{tot}} \quad (3)$$

$$P_{abs}^{dust} = \frac{\kappa_{abs}^{dust}}{\kappa_{tot}} \quad (4)$$

The dust scattering only changes the traveling directions of photon packets. Once the photon is absorbed by a dust grain, it is re-emitted as IR photons without further impact on the successive radiative transfer process. This technique is also used in other MCRT codes, like MOCASSIN^{3D} (Ercolano et al. 2005).

We adopt the fully sampled stellar population to obtain the shape of the ionizing spectrum and scale it to match with the desired ionizing photon rate. The stellar ionizing spectrum is generated by STARBURST99 with a continuous star formation history with a constant star formation rate of $1 M_{\odot} \text{ yr}^{-1}$ over a timescale of 5 Myr. We adopt a Salpeter initial mass function (IMF, Salpeter 1955) and the Geneva stellar evolution track (Lejeune & Schaerer 2001) with the Wolf-Rayet atmosphere library of Schmutz et al. (1992). The stellar abundance is aligned with the gas-phase metallicity by the same fractional solar abundance (Asplund et al. 2009). The ionizing source is placed at the center of the domain and the total luminosity of the ionizing source is set to be $10^{40} \text{ erg s}^{-1}$.

2.3. Dust grains

The composition of different sized dust grain is the key factor to determine the absorption and scattering contribution of dust. The grain size distribution is the balance of the processes relevant to the dust destruction and formation. We adopt the grain distribution proposed by Mathis et al. (1977),

$$dN(a)/da = ka^{-\alpha}, \quad (5)$$

where $N(a)$ is the number density of the dust grain at the size a , and α is selected to be 3.5.

In the dusty HII regions, the heavy elements are depleted from the gas-phase ISM and incorporated into the dust grains. The atomic depletion pattern is a factor constraining the dust

¹ <https://github.com/Jinyifei/M3>

attenuation (Salim & Narayanan 2020). We adopt the uniform depletion factor given by Jenkins (2009) for the model grids with varying metallicity, although Savage & Sembach (1996) has pointed out that the dust depletion is dependent on the ISM environment. Because the fractional depletion does not change with the metallicity of the gas, the gas-to-dust mass ratio in these models is only proportional to the gas-phase metallicity.

3. Dust Attenuation of Emission-Lines

We produce the 2D emission-line maps from the 3D data cube by integrating the emission-line fluxes reddened by the dust attenuation along the line-of-the-sight (LOS). The dust attenuation is constrained by the color excess $E(B - V)$ and the dust attenuation curve. We first derive the color excess $E(B-V)$ cube from the density field by assuming that a constant ratio between the $E(B-V)$ and the hydrogen column density, N_H ,

$$E(B - V)/N_H = \frac{4 \times 10^{-22} \text{ cm}^{-2}}{2.040685 \text{ mag}}, \quad (6)$$

which is adapted from Zucker et al. (2021) and Draine (2009). The $N_H = n_H \times dr$ is the column density of the cell with volume number density of n_H and size dr . This is the reverse approach of deriving the 3D density field of the Local Bubble (O'Neill et al. 2024) from the 3D dust attenuation map (Edenhofer et al. 2024).

The attenuation A_λ sensed by the i^{th} cell is the integration of the attenuation of the j^{th} cells on the line-of-the-sight, which is derived by:

$$A_\lambda^i = \sum_j E(B - V)_j \cdot x(\lambda), \quad (7)$$

where A_λ^i is the integrated attenuation of the i^{th} cell, $E(B - V)_j$ is the color excess of the j^{th} cell, and $x(\lambda)$ is the intrinsic extinction curve, which is the curve proposed by Fitzpatrick (1999).

The final projected 2D emission-line map is the integration of the dust reddened emission-line fluxes along the LOS:

$$f_\lambda^{\text{proj}} = \sum_i f_\lambda^i \times 10^{-0.4 \times A_\lambda^i}, \quad (8)$$

where the f_λ^{proj} is the projected line flux at the wavelength λ , and the f_λ^i is the intrinsic flux in the i^{th} cell.

Figure 1 and 2 present the projected $E(B-V)$ maps of the turbulent models. The $E(B-V)$ values scatter within each model because of the density fluctuation of the turbulent ISM. The fluctuation of the $E(B-V)$ map increases as the increasing Mach number of the turbulence. The $E(B-V)$ maps of the $k = 4$ models are more filamentary than the $k = 9$ models.

4. The Hydrogen Lines

We compute the Hydrogen lines from the Lyman series (energy level $n = 1$) to the Further series (energy level $n = 6$) based on the hydrogen recombination coefficients given by Storey & Hummer (1995). The transfer of the hydrogen resonance lines is assumed to be a linear combination of the Case A and the Case B conditions, based on the local temperature and density (Sutherland & Dopita 1993; Jin & Raymond 2025).

In Figure 1 and 2, we present the projected $H\beta$ maps of the turbulent models with varying Mach numbers and k parameters. In the low Mach number models, the density field of the HII region is smooth so the $H\beta$ distribution is close to the HII region

with the smooth spherical geometry. In the high Mach number models, the density field of the HII region becomes clumpy as the contrast between the low-density and high-density clumps is getting large. The $H\beta$ map of the HII region presents the bright clouds and the $H\beta$ brightness shows non-symmetric fluctuation. The boundary of the HII regions is fractal because the ionization front is broken into fragmental by the dense clumps.

The k parameter affects the morphology of HII regions by controlling the filamentary structures in the turbulent box. We note in passing that it is expected that the heating and expansion flow caused by the HII region evolution may modify the turbulent spectrum of the initial cold starforming gas, although this short experiment should prove indicative of the effects of ‘clumpiness’ compared to previous smooth symmetrical models. In a fixed-sized box, the larger k parameter breaks the large filaments into smaller pieces, increasing the degree of the clumpiness of the density field. For the HII regions with the same Mach number, the $k = 4$ models show more loops and filaments than the more uniform (on average) $k = 9$ models.

The probability distribution of the emissivity of the hydrogen recombination-lines is affected by Mach numbers through the PDF of the gaseous density. As shown in Figure 3, the PDFs of the emissivity of $H\beta$ are broader in the larger Mach-number turbulent boxes than those in the smaller Mach-number boxes of the same k parameter. This change is driven by the density variation within each HII region instead of the temperature variation because the PDF of electron temperature barely changes along with the Mach number of the turbulent medium.

The intrinsic $H\alpha/H\beta$ ratios vary within HII regions. Figure 3 also shows the probability distribution of the intrinsic $H\alpha/H\beta$ ratios within each HII region. The medium values of $H\alpha/H\beta$ ratio in the turbulent HII regions are between 3.02 and 3.03, deviated from the standard ‘‘Case B’’ value of 2.86. The PDFs of the $H\alpha/H\beta$ ratio have the similar shape between different Mach numbers. Within each HII region, 68.27 per cent of pixels have $H\alpha/H\beta$ ratios falling between 2.96 and 3.06. There is a subtle difference in the 3σ variation of PDF of the $H\alpha/H\beta$ ratio between the boxes of the same k parameter with different Mach numbers. The 3σ variation is enhanced in turbulence with the larger Mach numbers than the smaller Mach numbers for both $k = 4$ and 9 turbulence. As shown in Figure 4 and 5, these variations of $H\alpha/H\beta$ ratio are driven by electron temperature but independent of density, as seen in both the data and theoretical grids.

5. The Nebular Attenuation Curve

We derive the attenuation of the Hydrogen lines by comparing the attenuated line fluxes to their intrinsic fluxes.

$$A_\lambda^H = -2.5 \log_{10} \frac{F_\lambda^{\text{reddened}}}{F_\lambda^{\text{intrinsic}}},$$

where the F_λ is the flux of different Hydrogen lines, and the A_λ^H is the discrete attenuation at each hydrogen-line wavelength. Given we only consider the Hydrogen lines from the Lyman series to the Further series with 15 lines of each series, there are 90 sampling of the attenuation values as a function of the wavelength. We use the two-degree polynomial function to fit the full wavelength-dependent attenuation function.

$$A_\lambda = c_0 + c_1 \lambda^{-1} + c_2 \lambda^{-2},$$

The final nebular attenuation curve is formulated as below:

$$x(\lambda) = \frac{A_\lambda}{A_B - A_V} = \frac{A_\lambda}{E(B - V)},$$

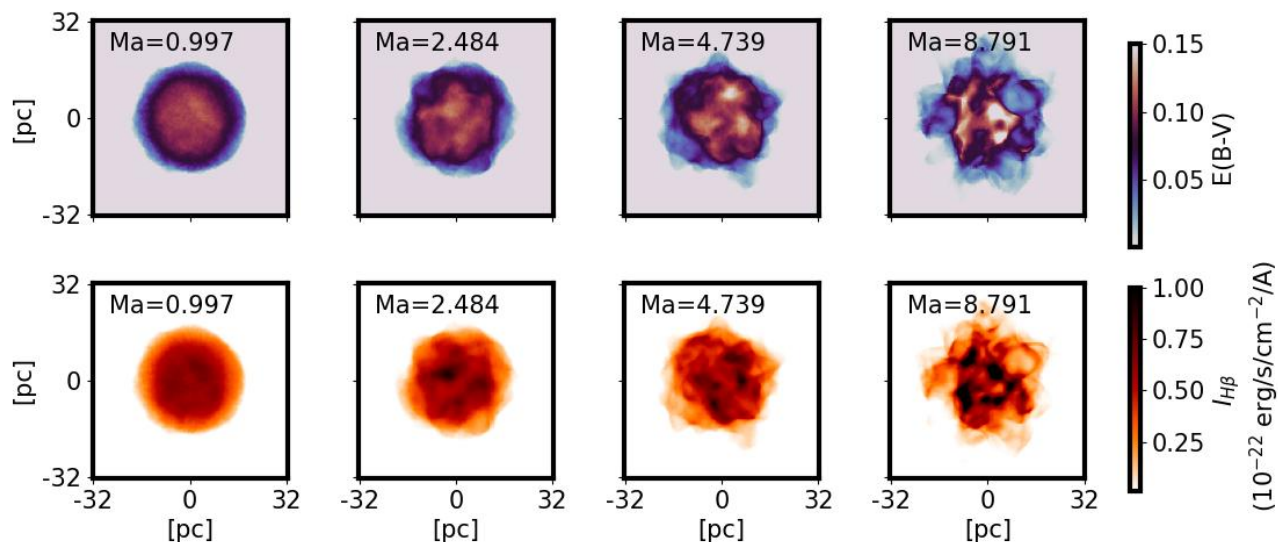


Fig. 1: The maps of the projected $E(B-V)$ and the attenuated $H\beta$ intensity of the $k = 4$ and $M=0.997, 2.484, 4.739, 8.791$ models.

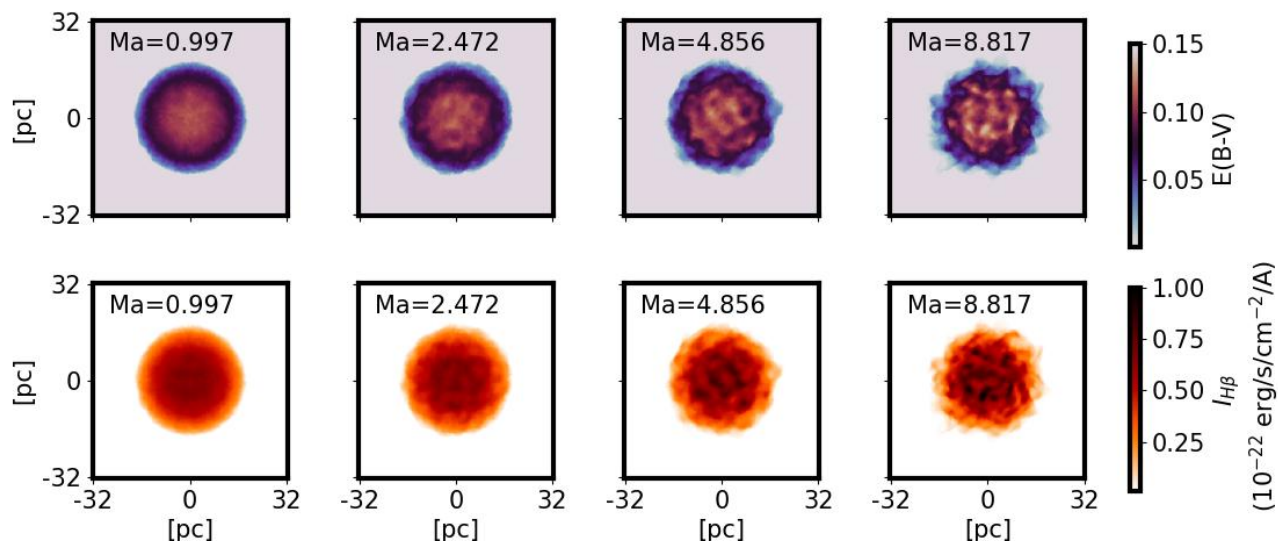


Fig. 2: Same to Figure 1 but for the $k = 9$ and $M=0.997, 2.472, 4.856, \text{ and } 8.817$ models.

where the A_λ is the fitted attenuation at the wavelength λ . We equate the A_V with the attenuation at 5500\AA and the A_B with the attenuation at 4400\AA . The fitted attenuation curves are shown in Figure 6 and the best-fit coefficients are listed in Table 1.

As shown in Figure 6, the A_λ values vary with the Mach number largely at the wavelength range shorter than $\lambda \lesssim 6600\text{\AA}$ ($1/\lambda \gtrsim 1.5\mu\text{m}^{-1}$) but remain similar at the long-wavelength range. This variation is caused by the change of the intrinsic $E(B-V)$ value of the ionized gas, which is more pronounced in the $k = 4$ turbulent boxes than in the $k = 9$ turbulent boxes, as shown in Table 2. After removing the effect of the varying $E(B-V)$, the derived attenuation curves of all the models, $x(\lambda)$, are consistent with the essential Fitzpatrick (1999) curve within the $1\text{-}\sigma$ uncertainty.

6. Discussion

In the photoionization models, the dust-to-gas ratio is always assumed to be a fixed value across the entire photoionized region (Dopita et al. 2000; Groves et al. 2004; Dopita et al. 2006b). We follow this assumption and select the dust-to-gas ratio in the ionized gas the same to the ratio in the neutral molecular clouds. Under this assumption, both the color excess, $E(B-V)$, and the emission-line intensity are proportional to the density of the total hydrogen atom. Although the column density and the dust covering factor vary with different Mach numbers in turbulent density fields, the heavy dust obscuration in one direction is canceled out by the high emissivity produced by the same groups of dense clouds. Therefore, the derived global attenuation curve has no pronounced dependence on the Mach number of the nebular internal turbulence.

Although the global attenuation is identical across boxes with different Mach numbers, the spatially-resolved projected at-

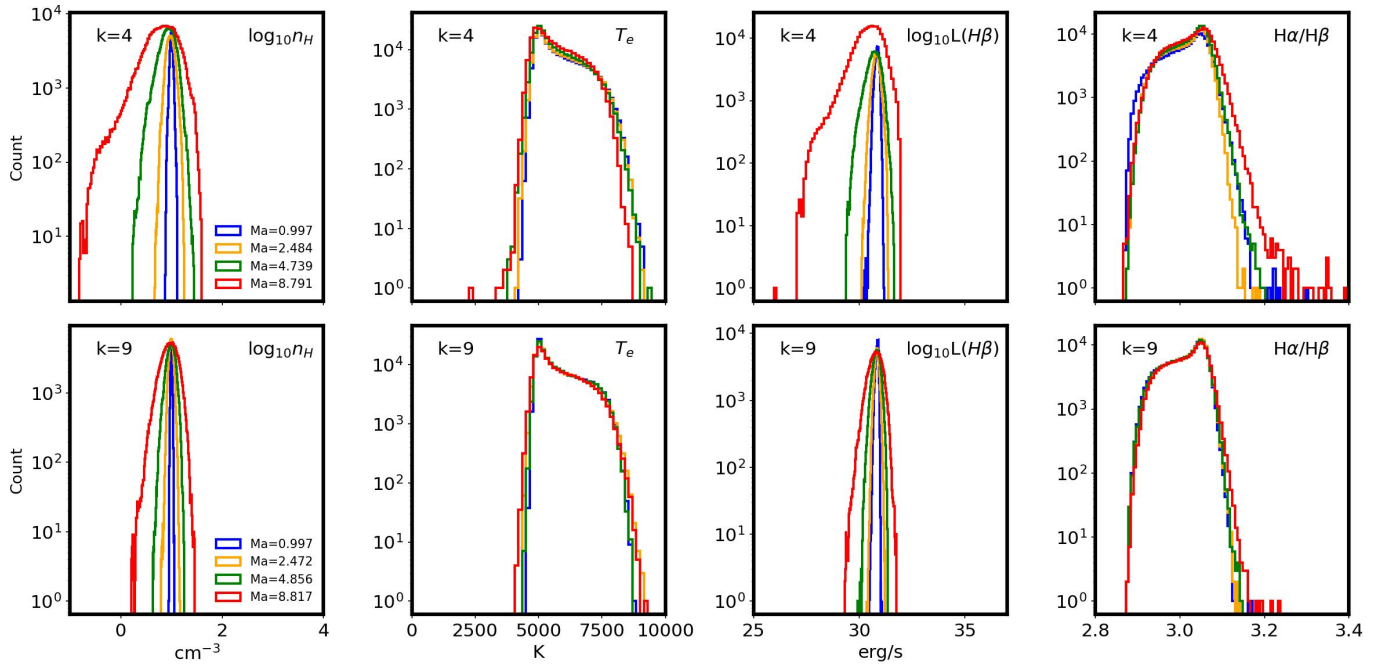


Fig. 3: The probability distribution function of the volume number density, n_H , the electron temperature, T_e , the $H\beta$ intensity, and the intrinsic $H\alpha/H\beta$ ratio of the HII regions of different Mach-number boxes.

Mach number	c_0	c_1	c_2	R_V
$k = 4$				
0.997	-5.702 ± 0.185	3.884 ± 0.183	-0.412 ± 0.045	3.589 ± 0.051
2.484	-5.707 ± 0.185	3.890 ± 0.183	-0.413 ± 0.045	3.593 ± 0.051
4.739	-5.710 ± 0.185	3.893 ± 0.183	-0.414 ± 0.045	3.594 ± 0.051
8.791	-5.720 ± 0.184	3.903 ± 0.183	-0.416 ± 0.045	3.604 ± 0.051
$k = 9$				
0.997	-5.695 ± 0.185	3.878 ± 0.184	-0.410 ± 0.045	3.584 ± 0.051
2.472	-5.697 ± 0.185	3.880 ± 0.183	-0.411 ± 0.045	3.586 ± 0.051
4.856	-5.706 ± 0.185	3.889 ± 0.183	-0.413 ± 0.045	3.592 ± 0.051
8.817	-5.711 ± 0.185	3.894 ± 0.183	-0.414 ± 0.045	3.596 ± 0.051

Table 1: Best-fit coefficients c_0, c_1, c_2 and derived R_V with 1σ errors for different Mach number turbulent boxes of $k = 4$ and 9.

attenuation maps reveal the density structures of the turbulence. The attenuation maps appear smooth in low-Mach-number boxes, where the density fluctuations are small, while more clumpy structures are shown in the high-Mach-number boxes. The attenuation maps also trace the shells and filaments present in the density fields. Particularly, the $\mathcal{M} = 8.791$, $k = 4$ attenuation map exhibits the bubble-like structures which arise from the interplay between the turbulent driving scale and the Mach number. These bubbles are seen in external galaxies (Watkins et al. 2023) and in our Milky-way, especially the Local Bubble (Zucker et al. 2021), which has been expanding over 14 Myrs (O’Neill et al. 2024).

In our models, we use the turbulent boxes without the contribution of gravity to generate the density fields. In galactic hydrodynamic simulations, gravity is a fundamental parameter to concentrate gas extending the high-density tail in the density probability function (Burkhart & Mocz 2019). This changes of density fluctuation may increase the 2D variations on attenuation maps but have subtle changes in the measurement of the global attenuation curve.

In our models, we ignore the dust drifting effect caused by the radiation pressure acting on the dust grains. Under the static equilibrium condition, the radiation pressure causes a radial gradient of the density within the ionized gas (Dopita et al. 2003, 2006a), compressing the dust and gas into an ionized shell, resulting in an elevated dust-to-gas ratio in the outer region of HII regions (Draine 2011). By including the dust drifting effect, the major fraction of the line emissivity is expected from the inner part of HII regions, separating from the attenuation of the dust whose large fraction resides at the outer part of HII regions. The action of the radiation pressure on dust will be discussed in the future version of M3D.

Apart from the internal dust attenuation of nebula, the observed flux suffers from the dust attenuation in-between the HII regions (Salim & Narayanan 2020). These inter-HII region space contributes the global dust attenuation without the high nebular emissivity. The radiative transfer models of dusty turbulent ISM have shown that the dusty clumps in the inter-HII region are one driver of the variation of the global attenuation curve in galaxies (Witt & Gordon 2000; Seon & Draine 2016).

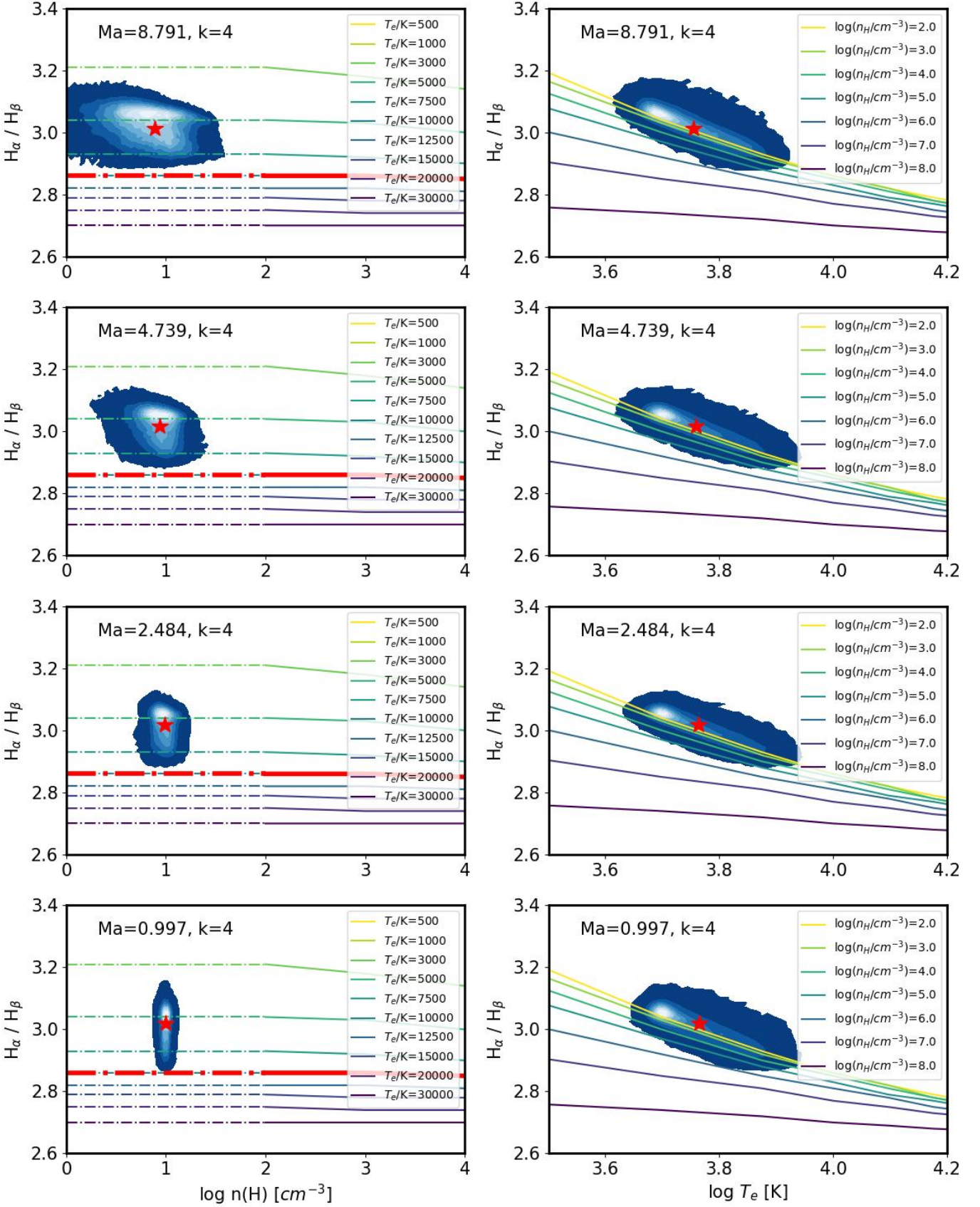
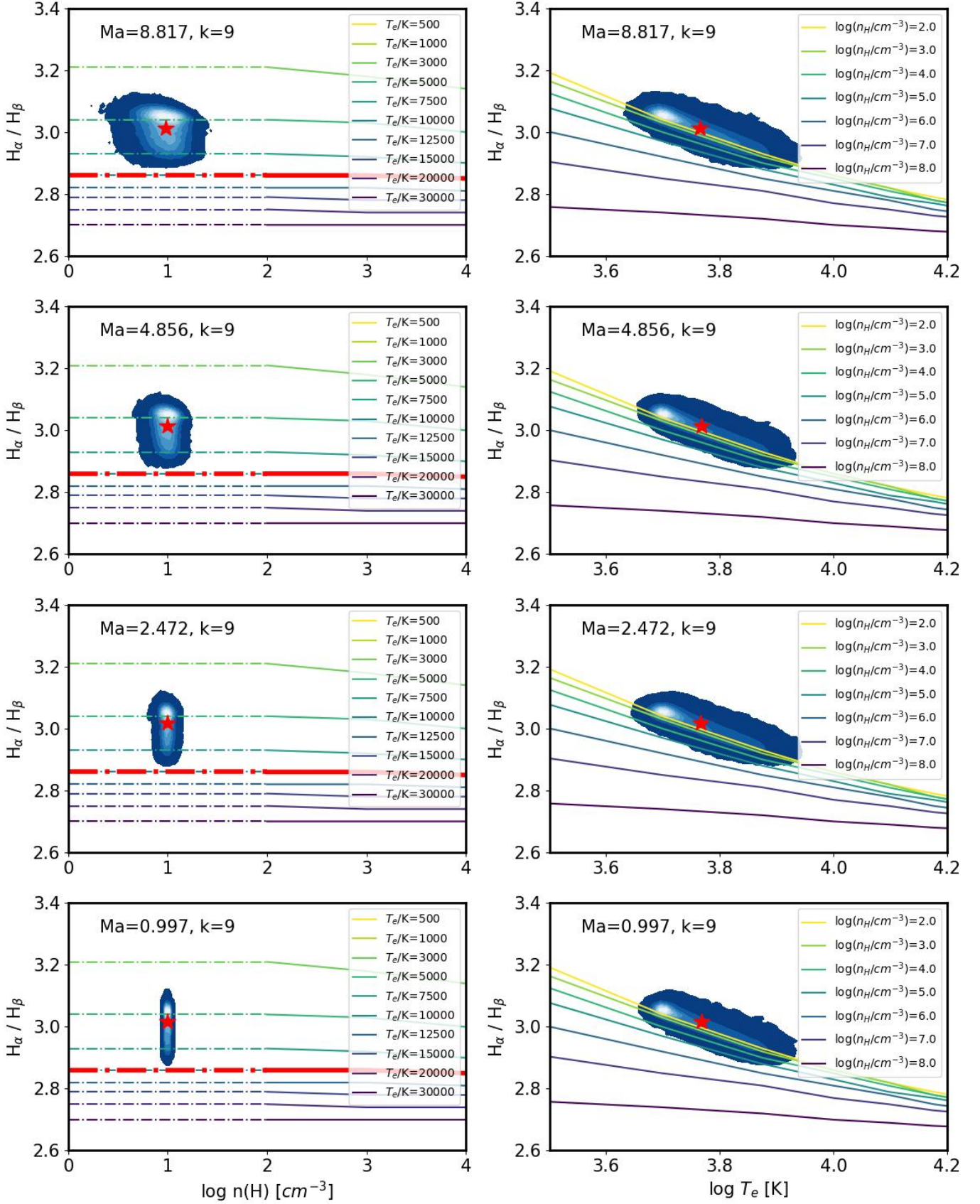


Fig. 4: The dependence of the intrinsic $H\alpha/H\beta$ ratio on the electron temperature and the gas density. The colored lines are the theoretical ratios in the Case B condition from the Appendix in Dopita & Sutherland (2003). The red thick line indicates the typical Case B $H\alpha/H\beta$ ratios at $T_e = 10,000$ K. The dashed line in the left panel are the exploration to the gas with density $n_H < 100$ cm⁻³. The color-filled contours are the $H\alpha/H\beta$ ratio of the turbulent box with Mach number $\mathcal{M} = 0.997, 2.484, 4.739$ and 8.791 . The k value is 4. The red star indicates the ratio of the integrated $H\alpha$ and $H\beta$ flux versus the average temperature and density.


 Fig. 5: The same figures as Figure 4 but for the $k = 9$ and $M=0.997, 2.472, 4.856,$ and 8.817 turbulent boxes.

Mach number	$E(B - V)_{\text{fit}}$	$E(B - V)_{\text{mean}}$
$k = 4$		
0.997	0.072 ± 0.001	0.076
2.484	0.071 ± 0.001	0.074
4.739	0.071 ± 0.001	0.070
8.791	0.069 ± 0.001	0.051
$k = 9$		
0.997	0.071 ± 0.001	0.077
2.472	0.071 ± 0.001	0.077
4.856	0.072 ± 0.001	0.075
8.817	0.072 ± 0.001	0.071

Table 2: Comparison of $E(B - V)_{\text{fit}}$ (with 1σ uncertainties) and mean $E(B - V)$ for $k = 9$ and $k = 4$ across Mach numbers. The values are extracted from the ionized gas only in photoionized models.

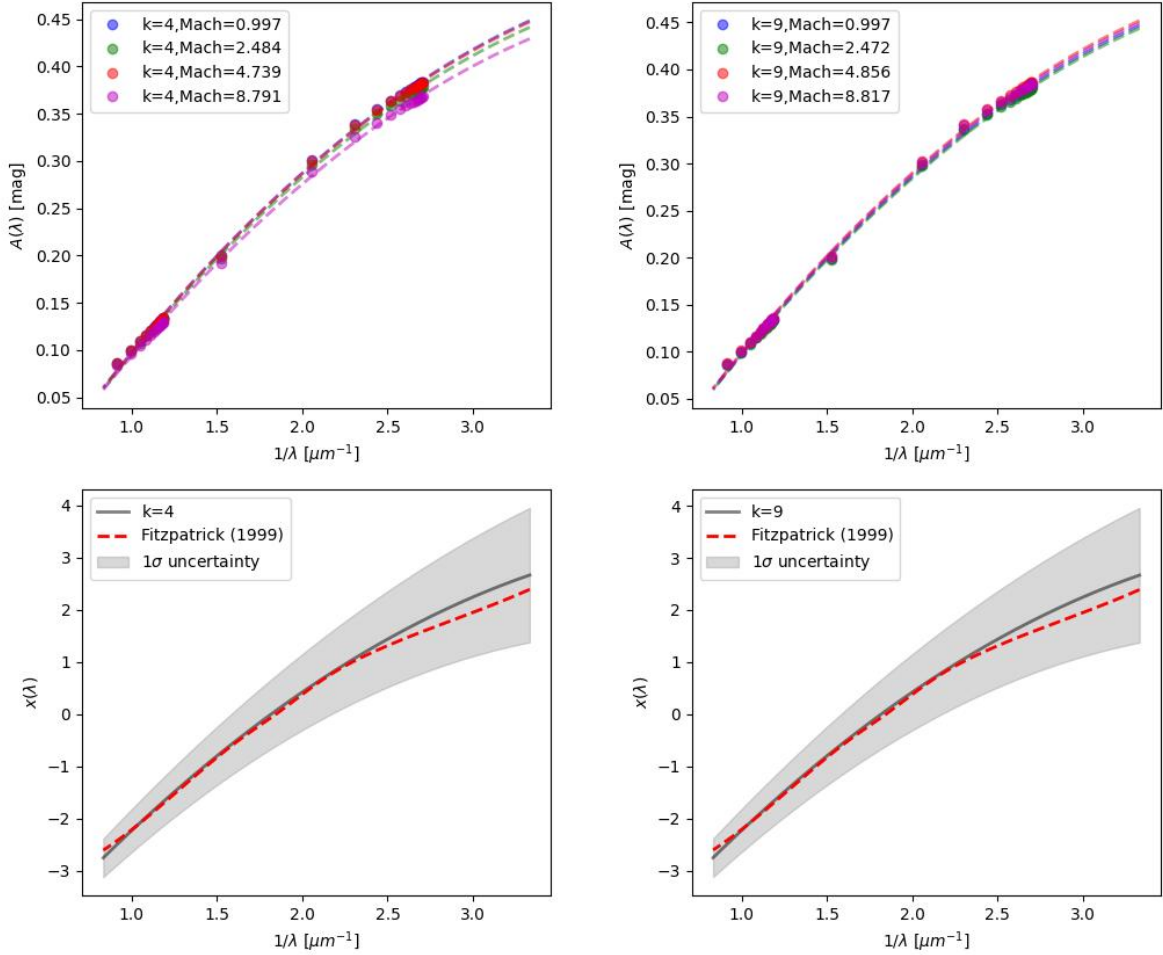


Fig. 6: **Upper:** The attenuation as a function of $1/\lambda$ for the $k = 4$ (left) and 9 (right) turbulent boxes. The dots are the attenuation values derived from individual Hydrogen lines by Equation 5 and the lines are the best-fit attenuation functions of different Mach number turbulent boxes. **Lower:** The derived attenuation curves for the $k = 4$ (left) and 9 (right) turbulent boxes. The black lines are the best-fit curves and the gray shades are the 1σ uncertainty areas of the fitting. The red dashed lines is the attenuation curve of the Fitzpatrick (1999).

The relative position of the HII regions and the dust in-between (so-called dust-star geometry) alters the slope of dust attenuation curve (Wild et al. 2011; Narayanan et al. 2018; Reddy et al. 2025). Our results further imply that the observed variation of the galactic-scale attenuation curve is caused by the dusty turbulent gas in-between the HII regions rather than the gas within the HII regions.

7. Conclusion

We implement the dust radiative transfer in the latest M3D code and produce the three-dimensional HII regions in the turbulent ISM with varying Mach numbers and wavenumbers. We derive the attenuation curve from the different series of Hydrogen lines of each HII region. We find the following conclusions.

- The intrinsic Hydrogen line ratios vary within the individual HII region because of the internal density fluctuation caused by turbulence. The global $H\alpha/H\beta$ ratio is around 3.02 to 3.03, deviating from the “Case B” assumption of 2.86. This value does not change with the varying Mach number turbulent structures.
- The clumpy and filament structures increase the attenuation of the HII region. However, the derived integrated selective attenuation curve is the same to the intrinsic input Fitzpatrick (1999) curve. The density fluctuation has no impact on the integrated attenuation curve of the turbulent HII region.
- The best-fit $E(B-V)$ is consistent with the mean $E(B-V)$ of the ionized gas. However, the mean $E(B-V)$ varies with Mach numbers and wavenumbers.

Our results highlight the consistency of the attenuation curves derived from the observed integrated emission-lines and the intrinsic curves, which is important for the future discussions of the dust attenuation of the nebulae in turbulent environments observed by the SDSS-V/LVM survey.

Acknowledgements. Y.F.J. acknowledges the computational resources at the Westlake High-Performance Computing Center. Y.F.J. and Y.S. acknowledge the support from the Startup funding of New-joined PI of Westlake University. This work is supported by the National Natural Science Foundation of China (NSFC grants 12141301, 12121003, 12333002). C.D. and Z.H. acknowledge support from DOE grant DE-SC0024639, the Alfred P. Sloan Research Fellowship, and the IBM Einstein Fellow Fund at the Institute for Advanced Study, Princeton. C.D. and Z.H. would like to acknowledge the high-performance computing support from National Energy Research Scientific Computing Center, a DOE Office of Science user facility.

References

Asplund, M., Grevesse, N., Sauval, A. J., & Scott, P. 2009, *ARA&A*, 47, 481
 Binette, L., Dopita, M. A., & Tuohy, I. R. 1985, *ApJ*, 297, 476
 Burkhart, B. & Mocz, P. 2019, *ApJ*, 879, 129
 Caplan, J. & Deharveng, L. 1986, *A&A*, 155, 297
 Del Zanna, G., Dere, K. P., Young, P. R., Landi, E., & Mason, H. E. 2015, *A&A*, 582, A56
 Dopita, M. A. 1976, *ApJ*, 209, 395
 Dopita, M. A., Fischera, J., Crowley, O., et al. 2006a, *ApJ*, 639, 788
 Dopita, M. A., Fischera, J., Sutherland, R. S., et al. 2006b, *ApJ*, 647, 244
 Dopita, M. A., Groves, B. A., Sutherland, R. S., & Kewley, L. J. 2003, *ApJ*, 583, 727
 Dopita, M. A., Kewley, L. J., Heisler, C. A., & Sutherland, R. S. 2000, *ApJ*, 542, 224
 Dopita, M. A. & Sutherland, R. S. 2003, *Astrophysics of the diffuse universe*
 Draine, B. T. 2009, in *Astronomical Society of the Pacific Conference Series*, Vol. 414, *Cosmic Dust - Near and Far*, ed. T. Henning, E. Grün, & J. Steinacker, 453
 Draine, B. T. 2011, *ApJ*, 732, 100
 Edenhofer, G., Zucker, C., Frank, P., et al. 2024, *A&A*, 685, A82

Elmegreen, B. G. & Scalo, J. 2004, *ARA&A*, 42, 211
 Ercolano, B., Barlow, M. J., & Storey, P. J. 2005, *MNRAS*, 362, 1038
 Fitzpatrick, E. L. 1999, *PASP*, 111, 63
 Groves, B. A., Dopita, M. A., & Sutherland, R. S. 2004, *ApJS*, 153, 9
 Hester, J. J., Scowen, P. A., Sankrit, R., et al. 1996, *AJ*, 111, 2349
 Jenkins, E. B. 2009, *ApJ*, 700, 1299
 Jin, Y., Kewley, L. J., & Sutherland, R. 2022a, *ApJ*, 927, 37
 Jin, Y., Kewley, L. J., & Sutherland, R. S. 2022b, *ApJ*, 934, L8
 Jin, Y. & Raymond, J. 2025, *ApJ*, 989, 203
 Kaasinen, M., Bian, F., Groves, B., Kewley, L. J., & Gupta, A. 2017, *MNRAS*, 465, 3220
 Lejeune, T. & Schaerer, D. 2001, *A&A*, 366, 538
 Mathis, J. S., Rumpl, W., & Nordsieck, K. H. 1977, *ApJ*, 217, 425
 Mellema, G., Arthur, S. J., Henney, W. J., Iliiev, I. T., & Shapiro, P. R. 2006, *ApJ*, 647, 397
 Molina, F. Z., Glover, S. C. O., Federrath, C., & Klessen, R. S. 2012, *MNRAS*, 423, 2680
 Narayanan, D., Conroy, C., Davé, R., Johnson, B. D., & Popping, G. 2018, *ApJ*, 869, 70
 Oey, M. S. & Kennicutt, Jr., R. C. 1997, *MNRAS*, 291, 827
 O’Neill, T. J., Zucker, C., Goodman, A. A., & Edenhofer, G. 2024, *ApJ*, 973, 136
 Pellegrini, E. W., Oey, M. S., Winkler, P. F., et al. 2012, *ApJ*, 755, 40
 Petrosian, V., Silk, J., & Field, G. B. 1972, *ApJ*, 177, L69
 Pillepich, A., Nelson, D., Springel, V., et al. 2019, *MNRAS*, 490, 3196
 Reddy, N. A., Shapley, A. E., Kriek, M., et al. 2020, *ApJ*, 902, 123
 Reddy, N. A., Shapley, A. E., Sanders, R. L., et al. 2025, *arXiv e-prints*, arXiv:2506.17396
 Salim, S. & Narayanan, D. 2020, *ARA&A*, 58, 529
 Salpeter, E. E. 1955, *ApJ*, 121, 161
 Sanders, R. L., Shapley, A. E., Jones, T., et al. 2021, *ApJ*, 914, 19
 Savage, B. D. & Sembach, K. R. 1996, *ARA&A*, 34, 279
 Schmutz, W., Leitherer, C., & Gruenwald, R. 1992, *PASP*, 104, 1164
 Seon, K.-I. & Draine, B. T. 2016, *ApJ*, 833, 201
 Shapley, A. E., Sanders, R. L., Topping, M. W., et al. 2025, *ApJ*, 980, 242
 Sparre, M., Whittingham, J., Damle, M., et al. 2022, *MNRAS*, 509, 2720
 Stone, J. M., Tomida, K., White, C. J., & Felker, K. G. 2020, *The Astrophysical Journal Supplement Series*, 249, 4
 Storey, P. J. & Hummer, D. G. 1995, *MNRAS*, 272, 41
 Sutherland, R., Dopita, M., Binette, L., & Groves, B. 2018, *MAPPINGS V: Astrophysical plasma modeling code*, *Astrophysics Source Code Library*, record ascl:1807.005
 Sutherland, R. S. & Dopita, M. A. 1993, *ApJS*, 88, 253
 Veilleux, S. & Osterbrock, D. E. 1987, *ApJS*, 63, 295
 Watkins, E. J., Barnes, A. T., Henny, K., et al. 2023, *ApJ*, 944, L24
 Wild, V., Charlot, S., Brinchmann, J., et al. 2011, *MNRAS*, 417, 1760
 Wisnioski, E., Förster Schreiber, N. M., Wuyts, S., et al. 2015, *ApJ*, 799, 209
 Witt, A. N. & Gordon, K. D. 2000, *ApJ*, 528, 799
 Wood, D. O. S. & Churchwell, E. 1989, *ApJS*, 69, 831
 Zamora-Avilés, M., Vázquez-Semadeni, E., González, R. F., et al. 2019, *MNRAS*, 487, 2200
 Zucker, C., Goodman, A., Alves, J., et al. 2021, *ApJ*, 919, 35